

Research Article

Preparation and Preliminary Nonlinear Optical Properties of BiFeO₃ Nanocrystal Suspensions from a Simple, Chelating Agent-Free Precipitation Route

Théo Tytus,¹ Oisín Phelan,¹ Mathias Urbain,¹ Gareth Clarke,¹ Jérémy Riporto,¹ Ronan Le Dantec,¹ Gnon Djanta,² Sandrine Beauquis,¹ Virginie Monnier,³ Yann Chevolut,³ Christine Galez,¹ and Yannick Mugnier¹

¹Univ. Savoie Mont Blanc, SYMME, F-74000 Annecy, France

²Faculté des Sciences, Université de LOME, Lomé, Togo

³Université de Lyon, Institut des Nanotechnologies de Lyon UMR CNRS 5270, Ecole Centrale de Lyon, 36 Avenue Guy de Collongue, F-69134 Ecully, France

Correspondence should be addressed to Yannick Mugnier; yannick.mugnier@univ-smb.fr

Received 15 May 2018; Accepted 3 July 2018; Published 9 September 2018

Academic Editor: Jean M. Greneche

Copyright © 2018 Théo Tytus et al. This is an open access article distributed under the Creative Commons Attribution License, which permits unrestricted use, distribution, and reproduction in any medium, provided the original work is properly cited.

Preparation of stable BiFeO₃ nanocrystal suspensions through a simple, low-cost precipitation technique is described. Amorphous precursors are first precipitated from metal nitrate salts in highly basic KOH solutions, and a short high-temperature annealing step is then performed to induce crystallization. Nanoparticles are characterized by X-ray diffraction (XRD), TEM, DLS and ζ-potential measurements, and the synthesis conditions optimized after a systematic variation of the KOH concentration within the range of 1–12 M. The presence of residual impurities (mainly Bi₂₅FeO₃₉ and Bi₂Fe₄O₉) quantified from XRD and mean nanocrystal size is found to be strongly influenced by the initial KOH solution content. A concentration at about 3–4 M is optimal in terms of BiFeO₃ phase-purity and nanocrystal size. Stability of aqueous dispersions of the amorphous precursors and of the purest crystallized nanoparticles is also characterized between pH=2 and pH=13. After preparation of stable, almost phase-pure BiFeO₃ nanocrystal suspensions, second and third harmonic scattering (SHS and THS) at excitation wavelengths of 1064 nm and 1250 nm are reported from nonlinear optical scattering measurements and compared with other recently published literature values.

1. Introduction

Bismuth ferrite (BiFeO₃) is today a well-known single-phase magnetoelectric material that combines room temperature ferroelectricity and antiferromagnetic ordering and as such, has attracted a considerable amount of attention due to its multiferroic properties [1, 2]. BiFeO₃ exhibits a rhombohedrally distorted perovskite structure (space group R3c) for which noncentrosymmetry arises from the rotation of the oxygen octahedrons around the pseudocubic [111] axis [3, 4]. Among potential applications based on bismuth ferrite, photocatalysis under ambient light [5], nonvolatile memory [6], spintronics [7, 8], and energy harvesting [9] can be mentioned as well as its increasing interest in bioimaging

due to intrinsic, very high second [10, 11] and third harmonic [12] properties. Harmonic nanoparticles (HNPs) [13] based on BiFeO₃ not only display a low cytotoxicity [14] but also display several “optical” advantages in terms of excitation wavelength tunability for deep-imaging [15], of photostability for long-term observations [16, 17], and of improved sensitivity due to specific harmonic signatures against endogenous signals [18–20].

Synthesis of BiFeO₃ nanoparticles has also been the subject of intense research, and several chemical routes that include, for instance, hydrothermal conditions [21–24], solvent evaporations [25], sol-gel polymerizations [26–29], sonochemical reactions, and microemulsion techniques [30] have already been studied. Hydrothermal syntheses with or

without chelating agents and sol-gel processes are indeed well-established approaches giving rise to phase-pure samples even if size- and shape-control in the case of BiFeO₃ are clearly issues [31], especially without use of expensive, microwave-assisted solvothermal conditions. Ideally, a facile, green, and scalable synthesis route which yields monodisperse and monocrystalline nanoparticles stabilized in aqueous solutions would be very convenient for the above-cited bioapplications, as it then allows surface modification of bare nanocrystals so as to improve their final biocompatibility and specificity for cell-targeting. To this end, we further explored the simple and cost-effective coprecipitation route already investigated [32–34] with the aim to prepare stable BiFeO₃ nanocrystal suspensions. Metal nitrate salts without any other organic additive and KOH solutions at different concentrations have been employed for the precipitation of the primary amorphous precursors. After a short annealing step at 720°C used here to promote crystallization and to inhibit as much as possible Ostwald ripening, it was found that an initial KOH concentration fixed at about 3–4 M is the best compromise in terms of size and residual impurities. The latter have been quantitatively assessed through Rietveld refinements for all the samples prepared from a KOH concentration varying between 1 M and 12 M. After optimization of the chemical synthesis, phase-pure nanopowders prepared at 4 M of KOH are dispersed in deionized water and stability of the resulting suspensions studied with DLS and ζ -potential measurements. Finally, a quantitative assessment of the averaged $\langle\chi^{(2)}\rangle$ susceptibility at 1064 nm under femtosecond laser excitation is compared with recently available literature values and discussed according to the synthesis process here developed. When the laser excitation wavelength is shifted to 1250 nm, preliminary optical characterizations indicate that the second and third harmonic scattering signals are easily monitored from ensemble measurements in the NIR biological transparency window.

2. Materials and Methods

For the preparation of BiFeO₃ nanocrystal suspensions, 1.58 mmol of bismuth pentahydrate (Bi(NO₃)₃·5H₂O, 0.77 g, Sigma-Aldrich, >98%) and stoichiometric amounts of iron nitrate nonahydrate (Fe(NO₃)₃·9H₂O, 0.64 g, Sigma-Aldrich, >99.9%) are weighed and dissolved without further purification in 3 mL of a 2 M nitric acid (HNO₃) solution. After dissolution of the precursors, the solution is slowly added into 17 mL of freshly prepared potassium hydroxide (KOH) solution of varying concentrations (between 0.1 M and 13 M) that is allowed to stir vigorously and continuously for 5 min. The as-obtained brownish precipitate is then treated for 1 h with a standard sonic bath, and the primary amorphous precipitate is finally collected by centrifugation at 15700 rpm. Five successive washings with deionized water and three more with ethanol are applied before a 12 h drying step at 85°C. The powder is then grounded with a mortar, carefully spread onto a thick alumina sample holder, and quickly annealed in air between 2 min 30 and 4 min, to promote crystallization at 720°C. Various amounts of crystallized powders can thus be obtained showing the scalability of

the chemical process. Stability studies and optical measurements were all performed from an initial mass concentration fixed at 1 mg/mL. Typically, 7 mg of dried powders were sonicated for 30 min in 7 mL of aqueous solutions (or in ethanol) and then left to settle for several days to allow sedimentation of the remaining aggregates. Finally, DLS measurements and weighing of the residual fraction (assuming spherical nanocrystals) allow to estimate the number density of nanocrystals in the supernatant at the end of the sedimentation period.

Physicochemical characterizations were carried out by XRD (using Co K α radiation from an INEL CPS 120 instrument and an acquisition time of 2 h per pattern and from a PANalytical X'Pert3 Powder diffractometer with a zero-background silicon sample holder), TEM (JEOL 2100 HT operating at 200 kV), and by ζ -potential and dynamic light scattering (DLS) measurements (Malvern Zetasizer Nano).

Nonlinear optical properties were measured by probing the second and third harmonic scattering signals as previously reported [12, 35, 36] except that the excitation source is here provided by a tunable (700–1300 nm) femtosecond Laser (Insight X3 Spectra-Physics) vertically polarized. SH and TH signals are collected perpendicularly to the fundamental beam and focused through two 5 cm focal length lenses onto the slit of a spectrometer (Andor Shamrock 193) combined to a CCD camera (Andor iDus 401 BVF). No analyser is used in the detection arm but a short pass filter to remove the excitation wavelength and a Dove prism to vertically rotate the image focal point along the spectrometer entrance slit.

3. Results

3.1. XRD Characterizations. As detailed in Materials and Methods, bismuth and iron nitrate precursors are first dissolved in 3 mL of 2 M nitric acid. Precipitation of the amorphous precursors is then obtained after mixing this acid precursor solution with 17 mL of a highly basic potassium hydroxide (KOH) solution of varying concentrations. To reduce as much as possible the amount of impurities after the calcination step, a homogeneous dispersion and concentration of the Fe³⁺ and Bi³⁺ ions is highly desirable and the local basic environment is to be stable enough during the precipitation process. We observed that addition of the KOH solution into the acid precursor one systematically results in very high impurity content (data not shown) whereas pouring the dissolved precursors into KOH solution under continuous stirring is much more favourable. In addition, a slow addition is vitally important as shown in Supplementary Material (Figure S1). A higher amount of the Bi-rich Bi₂₅Fe₃₉ phase is indeed present when the acid precursor solution is quickly poured whereas impurities are hardly visible for a drop-wise or very slow addition from a burette.

For a slow addition, amounts of impurities were also found to be very dependent on the initial KOH concentration that was allowed to vary between 0.1 M and 13 M. At 0.1 M of KOH, the XRD pattern indicates that α -Bi₂O₃ is the main crystallized phase produced after the short annealing step (data not shown). At higher KOH concentration, the BiFeO₃ phase is systematically obtained as the major phase, but the

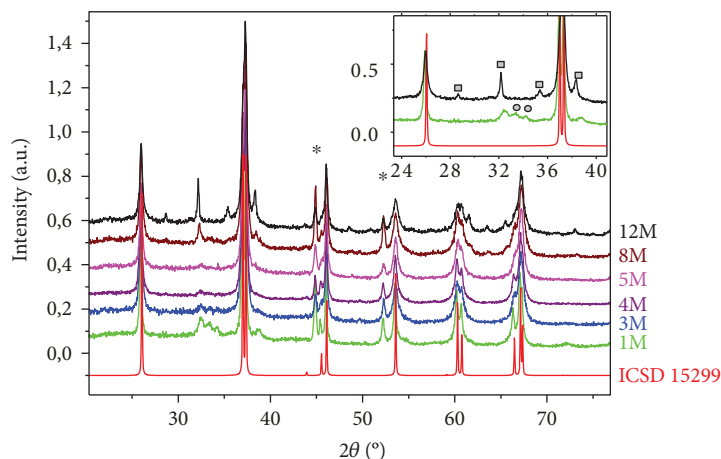


FIGURE 1: XRD patterns of BiFeO_3 samples depending on the initial amount of KOH and after 2 min 30 of annealing at 720°C . Peaks denoted as * belong to the aluminium sample holder. The BiFeO_3 reference profile (ICSD#15299) is shown in red at the bottom of the graph. Inset: peaks belonging to $\text{Bi}_{25}\text{FeO}_{39}$ (light gray square) and $\text{Bi}_2\text{Fe}_4\text{O}_9$ (light gray circle) are shown for the two most impure samples obtained at $\text{KOH} = 1\text{ M}$ and 12 M .

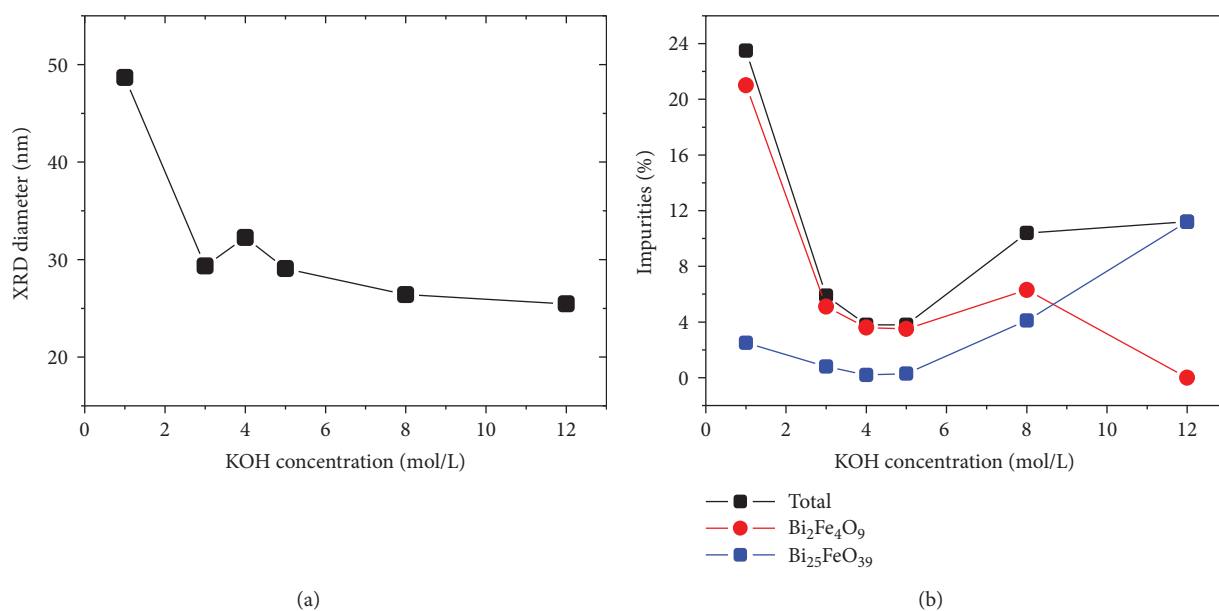


FIGURE 2: (a) Mean BiFeO_3 nanocrystal diameters obtained from the *Le Bail* fitting procedure versus initial KOH concentration used for precipitation. (b) Weight fraction of residual impurities ($\text{Bi}_{25}\text{FeO}_{39}$ and $\text{Bi}_2\text{Fe}_4\text{O}_9$) as derived from FullProf considering a structural model for each phase. Lines are a guide for the eye.

impurity content strongly varies as depicted in Figure 1. After the 2 min 30 crystallization step performed with 10 mg of amorphous precursors, residual impurities identified as $\text{Bi}_{25}\text{FeO}_{39}$ and $\text{Bi}_2\text{Fe}_4\text{O}_9$ are particularly visible in the low 2θ region, namely, between 30° and 40° of the diffraction patterns. A small amorphous contribution is also observed whatever the initial KOH concentration is. A zero-background sample holder has then been used in the following series of experiments to better investigate the amount of residual amorphous precursors and to eventually reduce their content.

For each sample, the mean diameter of BiFeO_3 nanocrystals is first derived after extraction of the integrated intensities within FullProf according to the *Le Bail* global fitting procedure [37]. Isotropic broadening of the diffraction peaks (without contribution of the Gaussian part in the FWHM) and the absence of residual strain are assumed. Quasi-spherical nanocrystals are thus considered for the final calculation of the mean diameter which is estimated below 40 nm in Figure 2(a) and with a trend to decrease when the KOH concentration is raised from 1 M to 12 M (see Figure S2 for the fitted profile of the sample precipitated at 3 M of KOH).

The mean crystallite size being derived, quantitative assessment of the weight fraction of the two impurity phases is then obtained from the scale factors after a full refinement (including structural models) of the XRD profiles within FullProf. The atomic positions from the ICSD files #15299, #68627, and #262861 corresponding to the BiFeO_3 , $\text{Bi}_{25}\text{FeO}_{39}$, and $\text{Bi}_2\text{Fe}_4\text{O}_9$ phases, respectively, are used as inputs and kept constant. Only the scale factors, cell parameters, and mean nanocrystal size of each phase are allowed to vary. In the case of BiFeO_3 , we noticed that assuming an anisotropic broadening improves to some extent the overall quality of the fits leading to slightly elongated particles along the [101] direction. The as-obtained mean diameters are still very consistent though with the ones plotted in Figure 2(a). Interestingly, the total amount of impurities in terms of weight fraction of the total mass shows in Figure 2(b) a well-defined minimum for the initial KOH concentration fixed at about 4–5 M. For the two corresponding samples, the mass fractions are found below 0.5% and 3.5% for the (heavy) Bi-rich $\text{Bi}_{25}\text{FeO}_{39}$ phase and the (light) Fe-rich $\text{Bi}_2\text{Fe}_4\text{O}_9$ phase, respectively. At 1 M of KOH, the total weight fraction for the two impurities attains 24% and reaches about 11% for the 12 M sample but with only the $\text{Bi}_{25}\text{FeO}_{39}$ phase present (see also Figure S3 for the fitted profiles of these two most impure samples).

3.2. Reproducibility and Scalability of the Chemical Process.

Larger numbers of BiFeO_3 amorphous precursors, namely, 20 mg, have also been annealed by using as before a small round alumina crucible (see Supplementary Material, Figure S4). A longer annealing period of 3 min, still at 720°C, is however necessary to promote crystallization without experimental evidence from the XRD profiles of a significant amorphous background arising from an incomplete crystallization (a cleaved-silicon zero-background sample holder is here used). When the initial KOH content is systematically varied in the range of 1–8 M, almost phase-pure BiFeO_3 nanocrystals are again produced at 3–4 M of KOH while the mean nanocrystal size obtained from Scherrer's formulae and the (012) reflection at $2\theta \sim 26.3^\circ$ again decreases as long as the initial KOH content is raised till 4 M (inset of Figure S4). It can be noticed though the absence of a Fe-rich phase in these syntheses since only the $\text{Bi}_{25}\text{FeO}_{39}$ and the trigonal metal Bi phases have been detected as residual impurities at high KOH content despite initial stoichiometric amounts of Bi and Fe.

For larger numbers of amorphous precursors, a flat alumina crucible has also been tested for which 40 mg of almost phase-pure ~ 30 nm nanocrystals could again be produced at 4 M of KOH and for a prolonged annealing time of 4 min at 720°C (see in Figure S5 the XRD patterns of BiFeO_3 samples depending on the initial amount of KOH). Comparatively to the thicker round crucible, the presence of impurity phases are more clearly visible at low and high KOH concentrations, but scalability of the chemical process is not prevented at 4 M of KOH. For an initial mass of precursors further increased at 200 mg, phase-purity and mean nanocrystal XRD size at ~ 30 nm have again been found in good agreement with previous results (Figure S6).

3.3. Suspension Stability. For the studies of the suspension stability, powders were all issued from the 200 mg precipitate obtained at 4 M of KOH, and mass concentration for both amorphous and crystallized particles was fixed at 1 mg/mL. Desired amounts of HNO_3 or KOH in deionized water were used to adjust the pH in the range of 2–13. Note that amorphous and crystallized particles dissolve very quickly at pH = 1 whereas they are chemically stable above pH = 2. As seen in Figure 3(a), ζ -potential measurements versus pH indicate an isoelectric point at pH ~ 5 for both amorphous and crystallized nanoparticles and that stability is better for the three samples dispersed at pH above 10. A ζ -potential value below -30 mV is then observed whereas the DLS size distribution by number is found to be centred at 90–100 nm for each sample. After a sedimentation period of 5 days, pictures included in Figure 3(a) are consistent with ζ -potential data (taken 3 days after the sonication process), especially the transparent vial at pH = 5 for which the absence of suspended particles can be noticed. Because of the size increase induced after calcination, nanocrystals are also found less stable than their amorphous counterpart. Only aqueous solutions with a pH fixed below 4 and above 9 are thus suitable (transparency of the supernatant shows no colour change after weeks) for any further surface chemical modification. Otherwise, nanocrystals are even more stable in ethanol. Regarding TEM imaging in Figure 3(b), amorphous powders precipitated at 4 M of KOH are composed of poorly shape-defined precursors of average size below ~ 10 nm.

After calcination, representative TEM images are shown in Figure 4 for the two samples precipitated at 3 M and 4 M of KOH (corresponding XRD patterns are given in Figure 1). The mean nanocrystal diameter is on average smaller for the 3 M sample, and nanocrystals are slightly elongated. The absence of morphology control can also be noticed which is consistent with the developed chelating agent-free chemical synthesis and short annealing step. In addition, if larger particle size can be expected from DLS measurements because of the measured hydrodynamic diameters, size distributions by number centred at 90–100 nm are significantly larger than the nanocrystal sizes derived from XRD as later discussed.

3.4. Preliminary NLO Properties. As previously reported [12, 35, 36], the orientation-averaged susceptibility

$\sqrt{\langle (\chi_{\text{NPs}}^{(2)})^2 \rangle} = \langle \chi_{\text{NPs}}^{(2)} \rangle$ of nanoparticles (NPs) from SHS measurements can be conveniently assessed by using a hyper-Rayleigh scattering configuration and through a two-step procedure. Briefly, the external reference method is first used with para-nitroaniline (pNA) molecules dissolved in methanol so as to calibrate the SH response of our experimental setup at 1064 nm under femtosecond excitation. For a nanocrystal suspension where V is the mean (DLS) nanocrystal size and N is the number density, the scattered SH signal can be expressed according to the excitation intensity I_ω as $I_{2\omega} = G \cdot N \cdot T_{2\omega} \langle (\chi_{\text{NPs}}^{(2)})^2 \rangle \cdot V^2 \cdot I_\omega^2$ where G includes the experimental collection efficiency and fundamental constants arising from a nonlinear radiating dipole. $T_{2\omega}$ is a reduction field factor allowing to

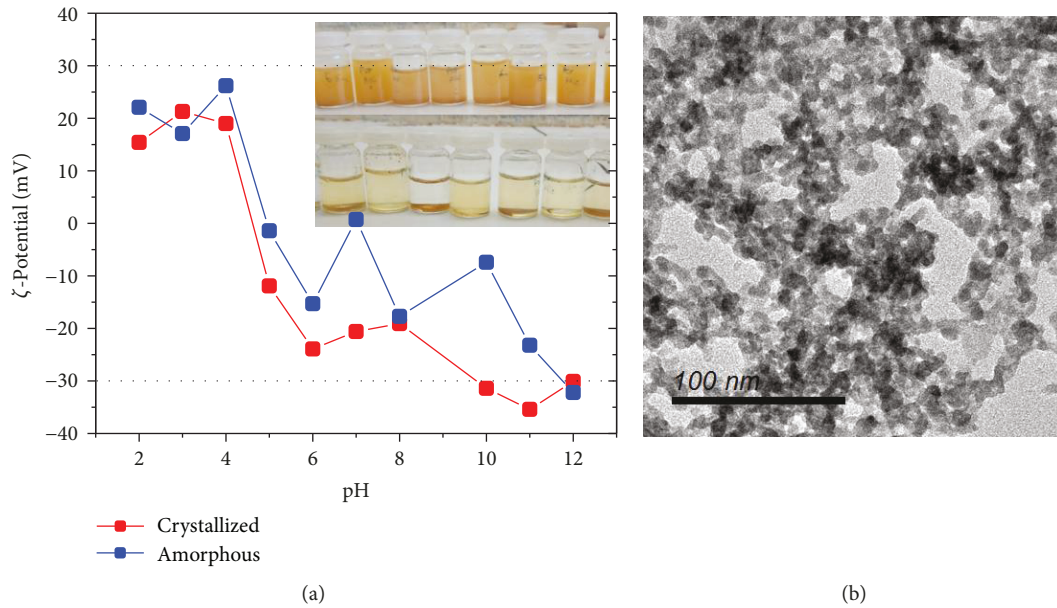


FIGURE 3: (a) ζ -Potential variations as a function of pH for amorphous precursors precipitated at $\text{KOH} = 4 \text{ M}$ (blue) and after crystallization (red). Inset: pictures taken just after dispersion (first row) and after a sedimentation period of 5 days (second row) for the crystallized powders dispersed at pH values fixed at 3.0, 4.0, 5.0, 6.0, 7.0, 8.0, and 10.0 (from left to right). (b) TEM image of the amorphous powders precipitated at $\text{KOH} = 4 \text{ M}$.

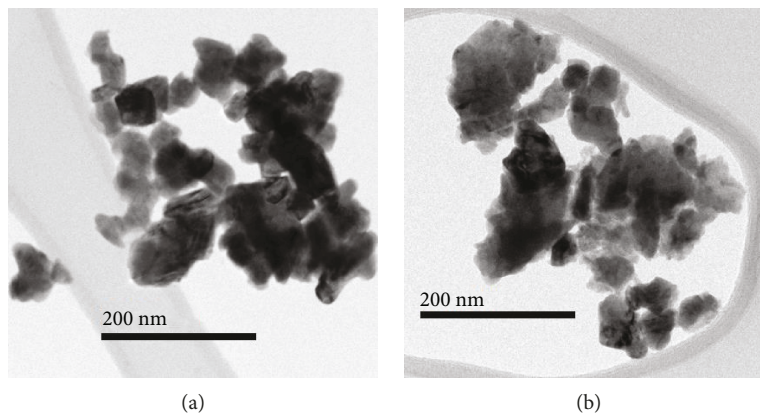


FIGURE 4: Representative TEM images of crystallized samples precipitated at 3 M (a) and 4 M (b) of KOH . Corresponding DLS sizes by number are centred at 90 nm and 100 nm, respectively.

describe the macroscopic field within the nanocrystal volume. For quasi-spherical nanocrystals $T_{2\omega} = (t_{\omega}^2 \cdot t_{2\omega})^2$ with $t_{\omega_i} = 3n_{\text{sol}}^2(\omega_i)/(2n_{\text{sol}}^2(\omega_i) + n_{\text{NPs}}^2(\omega_i))$ where $n_{\text{sol}}(\omega_i)$ and $n_{\text{NPs}}(\omega_i)$ stand for the solvent and nanoparticle average refractive index at ω_i , respectively.

Linear dependence of the SH signal versus the nanocrystal number density (N) after dilution of a stock solution with $N_0 = 2.75 \times 10^{11} \text{ cm}^{-3}$ is demonstrated in Figure 5(a). For a vertically polarized incident field and no analyser in the detection arm, the squared nanocrystal second-order susceptibility isotropically averaged over all orientations becomes $\langle (\chi_{\text{NPs}}^{(2)})^2 \rangle = \langle (\chi_{\text{XXX}}^{(2)})^2 \rangle + \langle (\chi_{\text{ZXX}}^{(2)})^2 \rangle = (6/35)\chi_{33}^2 + (32/105)\chi_{31}^2 + (8/21)\chi_{22}^2 + (44/105)\chi_{15}^2 + (4/21)\chi_{31}\chi_{33} + (4/35)\chi_{15}\chi_{33} + 16/105\chi_{15}\chi_{31}$ with $\{X, Y, Z\}$ the laboratory frame as defined in [35]. For a 90 nm DLS

size, the as-derived average SH coefficient is found to be $\langle d \rangle = \langle \chi_{\text{NPs}}^{(2)} \rangle / 2 = 60 \text{ pm/V}$ for a 1064 nm excitation.

Finally, shifting the excitation in the second NIR biological transparency window with a 1250 nm excitation wavelength has also been tested from ensemble measurements since BiFeO_3 nanocrystals recently emerged as an almost ideal candidate for tumour tissue labelling [19] and stem cell localization in the development of new therapeutic approaches [20]. Simultaneous acquisition and colocalization of the SH and TH signals indeed improve the imaging selectivity, but nonlinear efficiencies are not easily derived from imaging of individual, diffraction-limited nanocrystals. Polarization-resolved measures require complex mathematical fitting procedures whose expressions depend both on the nanocrystal orientation and the number of independent coefficients of the relevant crystal class and NLO order [12, 38].

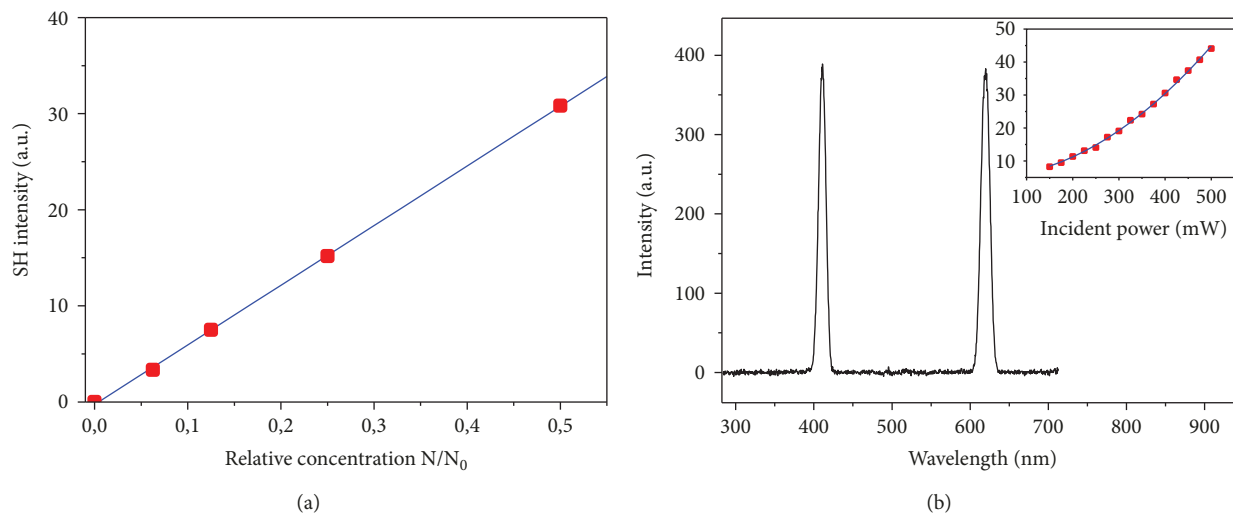


FIGURE 5: (a) Linear variation of the SH intensity according to the BiFeO_3 nanocrystal concentration at 1064 nm excitation. (b) Spectrally resolved trace confirming the only detection of SH and TH when the excitation wavelength is shifted to 1250 nm. Inset: quadratic dependence of the SH signal at 625 nm according to the excitation intensity.

Surprisingly, the TH signal emitted from individual BiFeO_3 nanocrystal has also been found well higher than the SH one in a recent study under tight focusing conditions when the excitation wavelength was further shifted to 1560 nm [39]. If high excitation intensities favour higher NLO orders, the above results obtained with microscopy approaches appeal for a full quantitative assessment of the wavelength-dependence of the SH and TH properties of BiFeO_3 . If this will be the topic of a forthcoming article, we here observed that preliminary ensemble measurements at 1250 nm under particular experimental conditions, namely, an average optical power adjusted at 500 mW and a focusing of the incident beam with a 5 cm focal length, results in SH (625 nm) and TH (417 nm) signals with very similar intensities as depicted in Figure 5(b). A full quantitative assessment of the orientation-averaged second- and third-order susceptibilities from ensemble measurements is thus readily achievable in the first two NIR transparency tissue windows (600–1000 nm and 1100–1350 nm).

4. Discussion and Concluding Remarks

Optimization of the coprecipitation conditions to prepare phase-pure BiFeO_3 nanocrystals was performed from amorphous precursors precipitated in very high alkaline KOH solutions of varying concentrations between 1 M and 12 M. Homogeneity of the reaction medium during precipitation has been found to be crucial because only slow addition of the acid solution containing the dissolved metal salts into a large volume of KOH under magnetic stirring results in XRD phase-pure powders. Comparatively to former studies for which precipitation was done from weaker alkaline solutions at pH=9 [32, 33] or at pH=12 [34], similar impurity phases (namely, $\text{Bi}_{25}\text{FeO}_{39}$ or its isomorph $\gamma\text{-Bi}_2\text{O}_3$ and $\text{Bi}_2\text{Fe}_4\text{O}_9$) were also observed but with a gradual disappearance as long as temperature of the 1 h calcination step was increased from 450°C to 500°C and to

600°C. A solid-state reaction between Bi-rich and Fe-rich phases was then proposed to account for the formation of pure BiFeO_3 at the highest temperature. In the present work, a very short annealing step of 3–4 min at 720°C is applied to induce crystallization well above the crystallization temperature of amorphous precursors found at 470–480°C from DTA analysis. Our results obtained from higher alkaline solutions and with a well shorter calcination time seem to indicate a different crystallization mechanism. First, if $\text{Fe}(\text{OH})_3$ and $\text{Bi}(\text{OH})_3$ are known to precipitate in alkaline media, a dissolution-crystallization mechanism is currently accepted for the preparation of pure BiFeO_3 under hydrothermal conditions [31]. Second, when crystallization is done in air, temperature-resolved XRD patterns of amorphous precursors indicate no evolution from RT till 425°C, but a local order seems already present after the RT precipitation as evidenced by two broad bands [33] (pp 2195) in the XRD patterns that we also observed (see Figure S7). Note that this local order is different from that of the characteristic 2-line ferrihydrite XRD response [40]. Last, solid state reactions are unlikely to occur between $\text{Bi}_{25}\text{FeO}_{39}$ and $\text{Bi}_2\text{Fe}_4\text{O}_9$ because these latter are slightly more thermodynamically stable than BiFeO_3 in the temperature range of 447°C–767°C [41]. A direct transformation from stoichiometric, amorphous precursors into crystalline BiFeO_3 could be an alternative as supported from our high-temperature short-annealing approach. It is our opinion that formation of the different impurity phases may rather be related to solubility issues and to the existence of amorphous bismuth(III)-iron(III) hydroxide solid-solutions as already evidenced in the case of chromium(III) and iron(III) [42]. This is supported by the following observations.

Solubility of amorphous $\text{Bi}(\text{OH})_3$ and crystalline $\alpha\text{-Bi}_2\text{O}_3$ in alkaline solutions is known to be identical leading to a concentration of Bi^{3+} ions below 10^{-5}M in 0.1 M NaOH solutions, but this concentration rapidly increases for stronger alkaline solutions [43]. In our experiments, $\alpha\text{-Bi}_2\text{O}_3$ is

the major phase when the KOH content is fixed at 0.1 M during precipitation whereas BiFeO_3 is the main compound in the 1–12 M range. On its side, solubility of ferrihydrite is even smaller with a minimum at $\text{pH} \sim 8$ and a concentration of Fe^{3+} varying from 10^{-10} M to 10^{-5} M as long as the pH is raised from 8 to 14 [44, 45]. Ferrihydrite is thermodynamically unstable and then transforms with time into either crystalline $\alpha\text{-FeO(OH)}$ (goethite) or $\alpha\text{-Fe}_2\text{O}_3$ (haematite) through a dissolution/reprecipitation mechanism or by dehydration, respectively, and this actually depends on the pH range and other parameters in strongly alkaline media [46]. Here, only traces of goethite have been found in our series of experiments at 8 M and 12 M of KOH and for an initial mass of 20 mg and 40 mg (see Figures S4 and S5).

It thus turns out from the above literature survey that Bi(III) oxide/hydroxide compounds and Fe(III) hydroxides have very similar solubilities in 1 M OH^- solutions, that solubility of bismuth ferrite is not known in aqueous solutions, and that precipitation in stronger alkaline solutions of stoichiometric amounts of Bi^{3+} and Fe^{3+} has, to the best of our knowledge, not yet been specifically investigated. On the other hand, the absence of the characteristic ferrihydrite signature among the amorphous precursors but that of a stable order till 425°C are to be considered so that the high-temperature short-annealing approach here developed supports the formation of amorphous bismuth(III)-iron(III) hydroxide solid-solutions for which stoichiometry is easily achieved at 3–4 M of KOH. Starting from high alkaline solutions, the homogeneous dispersion of the two metal cations in the stoichiometric amorphous precursors seems thus achievable because of solubility issues and more importantly, without use of any chelating agent whose effect is precisely to ensure this homogeneous dispersion in the traditional sol-gel chemistry routes [47].

Finally, the simple and low-cost chelating agent-free precipitation route here developed has however some drawbacks in terms of size- and shape-control of the as-produced nanocrystals. This is clearly demonstrated from the TEM observations. Regarding SH properties, the estimated average SH coefficient derived at $\langle d \rangle = 60$ pm/V is similar to the efficiency recently measured at 70 pm/V for BiFeO_3 nanocrystals obtained from the autocombustion method [11]. For monocrystalline and relatively well-monodisperse cubic-shape nanocrystals produced with mucic acid as the chelating agent, the averaged SH efficiency measured at 220 pm/V [48] is however significantly higher. This is in agreement with the eventual presence of residual amorphous precursors (Fe-rich and Bi-rich phases are not systematically observed here according to the KOH content), the formation of polycrystalline particles (the DLS size centred at 90–100 nm is well larger than the nanocrystal sizes derived from XRD) and the overall lack of well-defined size and shape particles whose polydispersity is known to decrease the orientation-averaged SH efficiency [36].

Data Availability

All the data are provided within the submitted files.

Conflicts of Interest

The authors declare no conflict of interest.

Authors' Contributions

YM and GC conceived and designed the experiments; TT and OP performed all the synthesis and most of the physical characterizations with the help of MU under the supervision of VM, SB, YC, CG, and YM; nonlinear optical measurements and modelling were achieved by JR and GD under the supervision of RLD; YM analysed the XRD results and wrote the paper.

Acknowledgments

We are very grateful to Jean-Christophe Marty (Laboratoire SYMME, Université Savoie Mont Blanc) for technical support. We gratefully acknowledge the financial support of the French-Switzerland Interreg V A program (project NANO-FIMT), of the French Agence Nationale de la Recherche (project RACINE), and of the 2015–2020 French Contrat Plan État Région (project E-TIME).

Supplementary Materials

Figure S1: XRD patterns in the low 2θ region showing the effect of a rapid/slow addition of a 4 M KOH solution on the final impurity content. Peaks belonging to the $\text{Bi}_{25}\text{FeO}_{39}$ (light gray square) are clearly more present when the acid precursor solution is quickly poured into KOH. Figure S2: zoom in the low 2θ region of a FullProf refinement with the *Le Bail* procedure (without structural model) applied to the XRD profile for the sample precipitated at 3 M of KOH. The excluded region at 45° is due to a parasitic reflection arising from the Al sample holder. Figure S3: representative FullProf refinements including structural models of the BiFeO_3 , $\text{Bi}_{25}\text{FeO}_{39}$, and $\text{Bi}_2\text{Fe}_4\text{O}_9$ phases for the two most impure samples obtained from an initial KOH content at 1 M and 12 M. Figure S4: XRD patterns of 20 mg BiFeO_3 samples depending on the initial amount of KOH and after 3 min of annealing at 720°C in a 1.5 mm thick alumina (round) crucible. Peaks denoted as * belong to the presence of the trigonal metal Bi phase (ICSD#64703) whereas light gray squares and open circles correspond to $\text{Bi}_{25}\text{FeO}_{39}$ and to the orthorhombic goethite Fe(OO)H phase (ICSD#71808), respectively. The BiFeO_3 reference profile (ICSD#15299) is shown in red at the bottom of the graph. Inset: mean crystallite size derived from the (012) reflection at $\sim 26.3^\circ$ and Scherrer's formulae after correction of the instrumental broadening. Figure S5: XRD patterns of 40 mg BiFeO_3 samples depending on the initial amount of KOH and after 4 min of annealing at 720°C in a larger alumina (flat) crucible. Peaks denoted as * belong to the presence of the trigonal metal Bi phase (ICSD#64703) whereas light gray squares and open circles correspond to $\text{Bi}_{25}\text{FeO}_{39}$ and to the orthorhombic goethite Fe(OO)H phase (ICSD#71808), respectively. The BiFeO_3 reference profile (ICSD#15299) is shown in red at the bottom of the graph. Figure S6: XRD pattern of a 200 mg BiFeO_3 sample

at 4 M of KOH after 4 min of annealing at 720°C in the large alumina (flat) crucible. Figure S7: XRD pattern of amorphous precursors precipitated at 4 M of KOH only showing diffraction peaks arising from the Al sample holder. (*Supplementary Materials*)

References

- [1] G. Catalan and J. F. Scott, "Physics and applications of bismuth ferrite," *Advanced Materials*, vol. 21, no. 24, pp. 2463–2485, 2009.
- [2] R. Safi and H. Shokrollahi, "Physics, chemistry and synthesis methods of nanostructured bismuth ferrite (BiFeO₃) as a ferroelectro-magnetic material," *Progress in Solid State Chemistry*, vol. 40, no. 1-2, pp. 6–15, 2012.
- [3] J. M. Moreau, C. Michel, R. Gerson, and W. J. James, "Ferroelectric BiFeO₃ X-ray and neutron diffraction study," *Journal of Physics and Chemistry of Solids*, vol. 32, no. 6, pp. 1315–1320, 1971.
- [4] I. Sosnowska, T. P. Neumaier, and E. Steichele, "Spiral magnetic ordering in bismuth ferrite," *Journal of Physics C: Solid State Physics*, vol. 15, no. 23, pp. 4835–4846, 1982.
- [5] F. Gao, X. Y. Chen, K. B. Yin et al., "Visible-light photocatalytic properties of weak magnetic BiFeO₃ nanoparticles," *Advanced Materials*, vol. 19, no. 19, pp. 2889–2892, 2007.
- [6] J. T. Heron, J. L. Bosse, Q. He et al., "Deterministic switching of ferromagnetism at room temperature using an electric field," *Nature*, vol. 516, no. 7531, pp. 370–373, 2014.
- [7] N. Balke, S. Choudhury, S. Jesse et al., "Deterministic control of ferroelastic switching in multiferroic materials," *Nature Nanotechnology*, vol. 4, no. 12, pp. 868–875, 2009.
- [8] D. Sando, A. Agbelele, D. Rahmedov et al., "Crafting the magnonic and spintronic response of BiFeO₃ films by epitaxial strain," *Nature Materials*, vol. 12, no. 7, pp. 641–646, 2013.
- [9] R. Moubah, O. Rousseau, D. Colson, A. Artemenko, M. Maglione, and M. Viret, "Photoelectric effects in single domain BiFeO₃ crystals," *Advanced Functional Materials*, vol. 22, no. 22, pp. 4814–4818, 2012.
- [10] A. Kumar, R. C. Rai, N. J. Podraza et al., "Linear and nonlinear optical properties of BiFeO₃," *Applied Physics Letters*, vol. 92, no. 12, article 121915, 2008.
- [11] S. Schwung, A. Rogov, G. Clarke et al., "Nonlinear optical and magnetic properties of BiFeO₃ harmonic nanoparticles," *Journal of Applied Physics*, vol. 116, no. 11, article 114306, 2014.
- [12] C. Schmidt, J. Riperto, A. Uldry et al., "Multi-order investigation of the nonlinear susceptibility tensors of individual nanoparticles," *Scientific Reports*, vol. 6, no. 1, article 25415, 2016.
- [13] A. Rogov, Y. Mugnier, and L. Bonacina, "Harmonic nanoparticles: noncentrosymmetric metal oxides for nonlinear optics," *Journal of Optics*, vol. 17, no. 3, article 033001, 2015.
- [14] D. Staedler, S. Passemard, T. Magouroux et al., "Cellular uptake and biocompatibility of bismuth ferrite harmonic advanced nanoparticles," *Nanomedicine: Nanotechnology, Biology and Medicine*, vol. 11, no. 4, pp. 815–824, 2014.
- [15] J. Extermann, L. Bonacina, E. Cuña et al., "Nanodoublers as deep imaging markers for multi-photon microscopy," *Optics Express*, vol. 17, no. 17, pp. 15342–15349, 2009.
- [16] D. Staedler, T. Magouroux, R. Hadji et al., "Harmonic nanocrystals for biolabeling: a survey of optical properties and biocompatibility," *ACS Nano*, vol. 6, no. 3, pp. 2542–2549, 2012.
- [17] L. Le Xuan, C. Zhou, A. Slablab et al., "Photostable second-harmonic generation from a single KTiOPO₄ nanocrystal for nonlinear microscopy," *Small*, vol. 4, no. 9, pp. 1332–1336, 2008.
- [18] P. Pantazis, J. Maloney, D. Wu, and S. E. Fraser, "Second harmonic generating (SHG) nanoprobe for in vivo imaging," *Proceedings of the National Academy of Sciences of the United States of America*, vol. 107, no. 33, pp. 14535–14540, 2010.
- [19] A. Rogov, M. Irondelle, F. Ramos Gomes et al., "Simultaneous multiharmonic imaging of nanoparticles in tissues for increased selectivity," *ACS Photonics*, vol. 2, no. 10, pp. 1416–1422, 2015.
- [20] L. Dubreil, I. Leroux, M. Ledevin et al., "Multi-harmonic imaging in the second near-infrared window of nanoparticle-labeled stem cells as a monitoring tool in tissue depth," *ACS Nano*, vol. 11, no. 7, pp. 6672–6681, 2017.
- [21] J.-T. Han, Y.-H. Huang, X.-J. Wu et al., "Tunable synthesis of bismuth ferrites with various morphologies," *Advanced Materials*, vol. 18, no. 16, pp. 2145–2148, 2006.
- [22] H. Zhang and K. Kajiyoshi, "Hydrothermal synthesis and size-dependent properties of multiferroic bismuth ferrite crystallites," *Journal of the American Ceramic Society*, vol. 93, no. 11, pp. 3842–3849, 2010.
- [23] S. H. Han, K. S. Kim, H. G. Kim et al., "Synthesis and characterization of multiferroic BiFeO₃ powders fabricated by hydrothermal method," *Ceramics International*, vol. 36, no. 4, pp. 1365–1372, 2010.
- [24] Y. Wang, G. Xu, Z. Ren et al., "Low temperature polymer assisted hydrothermal synthesis of bismuth ferrite nanoparticles," *Ceramics International*, vol. 34, no. 6, pp. 1569–1571, 2008.
- [25] S. Ghosh, S. Dasgupta, A. Sen, and H. Sekhar Maiti, "Low-temperature synthesis of nanosized bismuth ferrite by soft chemical route," *Journal of the American Ceramic Society*, vol. 88, no. 5, pp. 1349–1352, 2005.
- [26] M. Popa, D. Crespo, J. M. Calderon-Moreno, S. Preda, and V. Fruth, "Synthesis and structural characterization of single-phase BiFeO₃ powders from a polymeric precursor," *Journal of the American Ceramic Society*, vol. 90, no. 9, pp. 2723–2727, 2007.
- [27] H. Yang, T. Xian, Z. Q. Wei, J. F. Dai, J. L. Jiang, and W. J. Feng, "Size-controlled synthesis of BiFeO₃ nanoparticles by a soft-chemistry route," *Journal of Sol-Gel Science and Technology*, vol. 58, no. 1, pp. 238–243, 2011.
- [28] S. M. Selbach, M. Einarsrud, T. Tybell, and T. Grande, "Synthesis of BiFeO₃ by wet chemical methods," *Journal of the American Ceramic Society*, vol. 90, no. 11, pp. 3430–3434, 2007.
- [29] E. C. Aguiar, M. A. Ramirez, F. Moura, J. A. Varela, E. Longo, and A. Z. Simões, "Low-temperature synthesis of nanosized bismuth ferrite by the soft chemical method," *Ceramics International*, vol. 39, no. 1, pp. 13–20, 2013.
- [30] N. Das, R. Majumdar, A. Sen, and H. S. Maiti, "Nanosized bismuth ferrite powder prepared through sonochemical and microemulsion techniques," *Materials Letters*, vol. 61, no. 10, pp. 2100–2104, 2007.
- [31] Q. Zhang, D. Sando, and V. Nagarajan, "Chemical route derived bismuth ferrite thin films and nanomaterials," *Journal of Materials Chemistry C*, vol. 4, no. 19, pp. 4092–4124, 2016.
- [32] S. Shetty, V. R. Palkar, and R. Pinto, "Size effect study in magnetoelectric BiFeO₃ system," *Pramana*, vol. 58, no. 5-6, pp. 1027–1030, 2002.

- [33] H. Ke, W. Wang, Y. Wang et al., "Factors controlling pure-phase multiferroic BiFeO₃ powders synthesized by chemical co-precipitation," *Journal of Alloys and Compounds*, vol. 509, no. 5, pp. 2192–2197, 2011.
- [34] M. Y. Shami, M. S. Awan, and M. Anis-ur-Rehman, "Phase pure synthesis of BiFeO₃ nanopowders using diverse precursor via co-precipitation method," *Journal of Alloys and Compounds*, vol. 509, no. 41, pp. 10139–10144, 2011.
- [35] R. Le Dantec, Y. Mugnier, G. Djanta et al., "Ensemble and individual characterization of the nonlinear optical properties of ZnO and BaTiO₃ nanocrystals," *The Journal of Physical Chemistry C*, vol. 115, no. 31, pp. 15140–15146, 2011.
- [36] C. Joulaud, Y. Mugnier, G. Djanta, M. Dubled, and C. Galez, "Characterization of the nonlinear optical properties of nanocrystals by hyper Rayleigh scattering," *Journal of Nanobiotechnology*, vol. 11, Supplement 1, p. S8, 2013.
- [37] A. Le Bail, H. Duroy, and J. L. Fourquet, "Ab-initio structure determination of LiSbWO₆ by X-ray powder diffraction," *Materials Research Bulletin*, vol. 23, no. 3, pp. 447–452, 1988.
- [38] L. Bonacina, Y. Mugnier, F. Courvoisier et al., "Polar Fe(IO₃)₃ nanocrystals as local probes for nonlinear microscopy," *Applied Physics B: Lasers and Optics*, vol. 87, no. 3, pp. 399–403, 2007.
- [39] J. Riporto, A. Demierre, V. Kilin et al., "Bismuth ferrite dielectric nanoparticles excited at telecom wavelengths as multicolor sources by second, third, and fourth harmonic generation," *Nanoscale*, vol. 10, no. 17, pp. 8146–8152, 2018.
- [40] D. E. Janney, J. M. Cowley, and P. R. Buseck, "Transmission electron microscopy of synthetic 2-and 6-line ferrihydrite," *Clays and Clay Minerals*, vol. 48, no. 1, pp. 111–119, 2000.
- [41] T. Rojac, A. Bencan, B. Malic et al., "BiFeO₃ ceramics: processing, electrical, and electromechanical properties," *Journal of the American Ceramic Society*, vol. 97, no. 7, pp. 1993–2011, 2014.
- [42] B. M. Sass and D. Rai, "Solubility of amorphous chromium (III)-iron (III) hydroxide solid solutions," *Inorganic Chemistry*, vol. 26, no. 14, pp. 2228–2232, 1987.
- [43] D. Rai, M. Yui, H. T. Schaef, and A. Kitamura, "Thermodynamic model for BiPO₄(cr) and Bi(OH)₃(am) solubility in the aqueous Na⁺-H⁺-H₂PO₄⁻-HPO₄²⁻-PO₄³⁻-OH⁻-Cl⁻-H₂O system," *Journal of Solution Chemistry*, vol. 39, no. 7, pp. 999–1019, 2010.
- [44] X. Liu and F. J. Millero, "The solubility of iron hydroxide in sodium chloride solutions," *Geochimica et Cosmochimica Acta*, vol. 63, no. 19-20, pp. 3487–3497, 1999.
- [45] A. Stefa and Å. Nsson, "Iron (III) hydrolysis and solubility at 25°C," *Environmental Science & Technology*, vol. 41, no. 17, pp. 6117–6123, 2007.
- [46] R. M. Cornell, R. Giovanoli, and W. Schneider, "Review of the hydrolysis of Iron(III) and the crystallization of amorphous iron(III) hydroxide hydrate," *Journal of Chemical Technology & Biotechnology*, vol. 46, no. 2, pp. 115–134, 1989.
- [47] A. E. Danks, S. R. Hall, and Z. Schnepp, "The evolution of 'sol-gel' chemistry as a technique for materials synthesis," *Materials Horizons*, vol. 3, no. 2, pp. 91–112, 2016.
- [48] G. Clarke, A. Rogov, S. Mccarthy et al., "Preparation from a revisited wet chemical route of phase-pure, monocrystalline and SHG-efficient BiFeO₃ nanoparticles for harmonic bio-imaging," *Scientific Reports*, vol. 8, no. 1, article 10473, 2018.



Hindawi
Submit your manuscripts at
www.hindawi.com

